nature photonics

SUPPLEMENTARY INFORMATION

https://doi.org/10.1038/s41566-020-0667-0

In the format provided by the authors and unedited.

Organic light emitters exhibiting very fast reverse intersystem crossing

Yoshimasa Wada, Hiromichi Nakagawa, Soma Matsumoto, Yasuaki Wakisaka and Hironori Kaji ✉

Institute for Chemical Research, Kyoto University, Uji, Kyoto, Japan. ✉e-mail: kaji@scl.kyoto-u.ac.jp

Supplementary Information

Organic light emitters exhibiting very fast reverse intersystem crossing

Yoshimasa Wada, Hiromichi Nakagawa, Soma Matsumoto, Yasuaki Wakisaka, and Hironori Kaji

Institute for Chemical Research, Kyoto University, Uji, Kyoto 611-0011, Japan

Supplementary Text

Material synthesis and characterization

General procedure for material characterization

^{1}H and ^{13}C NMR spectra were recorded with a Bruker Avance-III (800 MHz for ^{1}H and 201 MHz for ^{13}C). The spectrometer was equipped with a 5-mm CPTCI triple resonance inverse detection cryoprobe. Chemical shifts are reported in δ ppm, using residual protons in deuterated solvents for ^{1}H NMR experiments and solvent peaks for ^{13}C NMR spectra as internal standards. CD_2Cl_2 was used for TpAT-tFFO and TpMAT-tFFO, whereas $CDCl_3$ was used for other compounds (Compound S1, Compound S2, and TpPXT-tFFO). All measurements were performed at 300 K; however, ^{13}C NMR spectrum of compound S2 was also measured at 263 K to clearly detect a broad ^{13}C resonance line linked to boronic ester at 124.77 ppm. Atmospheric pressure chemical ionization (APCI) mass spectra were measured with a Bruker micrOTOF-Q II (Bruker, Germany). Elemental analysis was conducted with a CHN analyser, MICRO CORDER JM10 (J-Science Lab Co., Ltd., Japan) and Flash Smart Organic Elemental Analyzers (Thermo Fisher Scientific Co., Ltd.). Melting points (T_m) were determined from the onset of the differential scanning calorimetry (DSC) curve measured with a DSC1 (METTLER TOLEDO) at a heating rate of 10 °C min^{-1}.

The synthesis scheme of TpAT-tFFO is summarized in Supplementary Scheme 1. The starting material, 1,8-dibromotriptycene, was prepared according to ref. S1.

Compound S1

A 60 mL portion of deoxidized toluene was added to a 100-mL round bottom Schlenk flask under Ar atmosphere, containing 1,8-dibromotriptycene (6.18 g, 15.1 mmol), 9,9-dimethyl-9,10-dihydroacridine (1.26 g, 6.03 mmol), $Pd_2(dba)_3{\cdot}CHCl_3$ (186 mg, 0.18 mmol), XPhos (172 mg, 0.36 mmol), and NaOtBu (1.15 g, 12.0 mmol). The mixture was stirred overnight at 120 °C. After the reaction mixture was cooled to ambient temperature, 20 mL of distilled water was added and the organic layer was extracted with 100 mL of ethyl acetate three times. The combined organics were dried over sodium sulfate, the crude mixture was concentrated under reduced pressure and then purified by silica gel column chromatography using hexane/dichloromethane = 4/1 as eluent. 2.37 g (4.40 mmol) of Compound S1 (Supplementary Scheme 1) was obtained in 73% yield.

Material Characterization

^{1}H NMR (800 MHz, $CDCl_3$, 300 K, δ): 7.55 (dd, J = 7.8, 1.4 Hz, 1H), 7.53 (d, J = 7.4 Hz, 1H), 7.50 (dd, J = 7.8, 1.4 Hz, 1H) , 7.42 (d, J = 7.3 Hz, 1H), 7.34 (d, J = 7.3 Hz, 1H), 7.24 (t, J = 7.6 Hz, 1H), 7.06 (dd, J = 7.9, 1.0 Hz, 1H), 7.02 (td, J = 7.3, 1.2 Hz, 1H), 6.98 (dd, J = 7.7, 0.9 Hz, 1H), 6.96–6.91 (4H), 6.84 (t, J = 7.6 Hz, 1H), 6.80 (ddd, J = 8.2, 7.0, 1.5 Hz, 1H), 6.78 (ddd, J = 8.2, 7.0, 1.5 Hz, 1H), 5.88 (dd, J = 8.2, 1.0 Hz, 1H), 5.77 (dd, J = 8.2, 1.0 Hz, 1H), 5.73 (s, 1H), 5.55 (s, 1H),

1.94 (s, 3H), 1.71 (s, 3H). ^{13}C NMR (201 MHz, $CDCl_3$, 300 K, δ):148.26, 147.71, 145.10, 144.78, 143.45, 143.09, 140.50, 140.07, 136.31, 129.80, 129.62, 128.91, 127.74, 127.70, 126.77, 126.58, 126.55, 125.55, 125.48, 125.39, 125.25, 125.14, 123.48, 123.43, 122.49, 120.65, 120.44, 119.94, 114.14, 114.12, 54.65, 48.52, 36.03, 32.82, 31.49.

APCI-MS (m/z): [M+H]+ calcd. for $C_{35}H_{27}BrN$, 540.1321; found, 540.1325. T_m = 196 °C.

Compound S2

In a 50-mL two-neck round bottom flask, Compound S1 (1.77 g, 3.27 mmol) was dissolved in 25 mL of dehydrated THF under an Ar atmosphere and the solution was cooled to −78 °C. Therein, 3 mL (4.80 mmol) of *n*-BuLi solution 1.6 M in hexane was slowly added with stirring. After 2 h stirring at −78 °C, 0.78 mL (3.87 mmol) of 2-isopropoxy-4,4,5,5-tetramethyl-1,3,2-dioxaborolane was added to the solution, and the reaction mixture was slowly warmed up to ambient temperature. The crude solution was quenched with 1 M HCl aqueous solution and the resulting mixture layer was extracted with 50 mL of ethyl acetate three times. The combined organic layers were further washed with brine and distilled water, and dried over sodium sulfate. The crude mixture was concentrated under reduced pressure and then purified by silica gel column chromatography using hexane/dichloromethane = 7/3 as eluent. 0.864 g (1.47 mmol) of Compound S2 (Supplementary Scheme 1) was obtained in 45% yield.

Material Characterization

For the ^{13}C NMR spectrum of compound S2, the broad ^{13}C resonance line linked to boronic ester was overlapped with another resonance lines at 125.02 and 125.04 ppm. Therefore, the ^{13}C NMR spectrum at 263 K is also shown, which contain a broad but well separated resonance line of the carbon at 124.77 ppm (see Supplementary Figures 5 and 6).

^{1}H NMR (800 MHz, $CDCl_3$, 300 K, δ): 7.51–7.49 (3H), 7.44–7.43 (2H), 7.35 (dd, J = 7.4, 1.2 Hz, 1H), 7.17 (t, J = 7.6 Hz, 1H), 7.15 (d, J = 7.3 Hz, 1H) , 7.03 (td, J = 7.3, 1.2, 1H), 7.02–6.96 (3H), 6.91 (ddd, J = 8.0, 7.1, 1.5 Hz, 1H), 6.87–6.85 (2H), 6.72 (ddd, J = 8.2, 7.1, 1.5 Hz, 1H), 6.32 (s, 1H), 6.05 (dd, J = 8.1, 1.1 Hz, 1H), 5.68 (dd, J = 8.2, 1.1 Hz, 1H), 5.57 (s, 1H), 1.96 (s, 3H), 1.44 (s, 3H), 0.94 (s, 3H), 0.81 (s, 6H). ^{13}C NMR (201 MHz, $CDCl_3$, 300 K, δ):150.78, 148.01, 146.76, 145.82, 145.19, 144.77, 141.14, 140.47, 136.52, 131.82, 130.75, 130.12, 127.88, 126.58, 126.57, 126.37, 126.10, 125.23, 125.04, 125.02, 124.41, 124.36, 124.27, 123.38, 123.33, 120.61, 120.42, 115.23, 114.70, 83.17, 54.63, 48.13, 36.09, 34.65, 25.88, 24.84, 24.55. ^{13}C NMR (201 MHz, $CDCl_3$, 263 K, δ):150.54, 147.79, 146.53, 145.61, 145.03, 144.52, 140.96, 140.31, 136.12, 131.59, 130.62, 129.94, 127.85, 126.48, 126.31, 126.14, 125.15, 125.02, 124.97, 124.77 124.31, 124.25, 124.23, 123.45, 123.34, 120.59, 120.35, 114.97, 114.49, 83.12, 54.27, 47.94, 36.01, 34.35, 25.45, 24.67, 24.55. APCI-MS (m/z): [M+H]+ calcd. for $C_{41}H_{39}BNO_2$, 588.3068; found, 588.3094. T_m = 318 °C.

TpAT-tFFO

A 60-mL portion of deoxidized toluene and 6.0 mL of 2 M aqueous potassium carbonate (12.0 mmol) were added to a 100-mL round bottom Schlenk flask containing **Compound S2** (0.85 g, 1.45 mmol), 2-chloro-4,6-diphenyl-1,3,5-triazine (0.58 g, 2.17 mmol), and $Pd(PPh_3)_4$ (168 mg, 0.15 mmol). After three freeze-pump-thaw cycles under an Ar atmosphere, the mixture was stirred at 120 °C for 24 h. After the reaction mixture was cooled to ambient temperature, 40 mL of distilled water was added and the organic layer was extracted with 50 mL of ethyl acetate three times. The combined organics were dried over sodium sulfate, concentrated under reduced pressure and then purified by column chromatography using hexane/dichloromethane = 4/1. 0.679 g (0.98 mmol) of TpAT-tFFO was obtained in 68% yield.

Material Characterization

^{1}H NMR (800 MHz, CD_2Cl_2, 300 K, δ): 8.47 (d, J = 7.5 Hz, 4H), 8.25 (dd, J = 7.8, 1.2 Hz, 1H), 7.70 (dd, J = 7.2, 1.2 Hz, 1H), 7.62−7.59 (3H) 7.55 (dt, J = 7.3 Hz, 0.5 Hz, 1H), 7.47 (t, J = 7.6 Hz, 4H), 7.28−7.25 (3H), 7.20 (s, 1H), 7.15 (dd, J = 7.7, 1.4 Hz, 1H), 7.11 (td, J = 7.3, 1.2 Hz, 1H), 7.05 (td, J = 7.3, 1.2 Hz, 1H), 6.96 (ddd, J = 7.6, 7.0, 1.2 Hz, 1H), 6.90 (dd, 7.6, 1.4 Hz, 1H), 6.87 (dd, 7.6, 1.1 Hz, 1H), 6.83 (m, 1H), 6.27 (m, 1H), 6.10 (dd, J = 7.6, 7.0, 1.2 Hz, 1H), 5.76 (dd, J = 8.1, 1.1 Hz, 1H), 5.74 (s, 1H), 5.54 (d, J = 8.0, 1.2 Hz, 1H), 1.24 (s, 3H), 1.09 (s, 3H). ^{13}C NMR (201 MHz, CD_2Cl_2, 300 K, δ): 172.43, 170.59, 148.27, 147.14, 145.70, 145.56, 144.61, 143.30, 140.34, 140.06, 135.95, 135.83, 132.45, 131.67, 129.67, 128.79, 128.32, 128.31, 127.69, 127.67, 126.60, 126.41, 125.82, 125.78, 125.20, 125.09, 124.96, 124.90, 124.38, 123.31, 123.25, 123.22, 120.45, 119.85, 113.69, 112.05, 54.28, 45.25, 35.33, 32.75, 23.23. APCI-MS (m/z): [M+H]+ calcd. for $C_{50}H_{37}N_4$, 693.3013; found, 693.3061; Elemental analysis calcd. (%) for $C_{50}H_{36}N_4$: C, 86.68; H, 5.24; N, 8.09; found: C, 86.93; H, 5.38; N, 8.04. Thermal stability: glass transition temperature (T_g) = 136 °C. T_m = 257 °C.

TpMAT-tFFO

Material Characterization

^{1}H NMR (800 MHz, CD_2Cl_2, 300 K, δ): 8.49 (d, J = 7.4 Hz, 4H), 8.36 (dd, J = 7.8, 1.3 Hz, 1H), 7.70 (dd, J = 7.2, 1.2 Hz, 1H), 7.60−7.57 (3H) 7.55 (dt, J = 7.3, 0.5 Hz, 1H), 7.43 (t, J = 7.6 Hz, 4H), 7.41 (s, 1H), 7.32 (dt, J = 7.3, 0.5 Hz, 1H), 7.28 (dd, J = 7.8, 7.2 Hz, 1H), 7.22 (t, J = 7.6 Hz, 1H), 7.12 (td, J = 7.3, 1.2 Hz, 1H), 7.07 (td, J = 7.3, 1.2 Hz, 1H), 6.93 (d, J = 1.2 Hz, 1H), 6.82 (dd, J = 7.6, 1.0 Hz, 1H), 6.70 (d, J = 1.2 Hz, 1H), 6.65 (dd, J = 8.1, 1.0 Hz, 1H), 6.05 (dd, J = 8.0, 1.0 Hz, 1H), 5.74 (s, 1H), 5.67 (d, J = 8.1 Hz, 1H), 5.40 (d, J = 8.1 Hz, 1H), 2.38 (s, 3H), 1.53 (s, 3H), 1.22 (s, 3H), 1.07 (s, 3H). ^{13}C NMR (201 MHz, CD_2Cl_2, 300 K, δ): 172.26, 170.34, 148.01, 147.29, 145.97, 145.63, 145.01, 143.44, 138.40, 138.07, 136.16, 135.91, 132.25, 131.59, 129.71, 129.06, 128.93, 128.84, 128.29, 128.23, 127.68, 127.63, 126.75, 126.46, 126.13, 125.74, 125.22, 125.13, 125.06,

124.93, 124.91, 124.54, 123.94, 123.21, 123.07, 113.52, 111.99, 54.32, 45.31, 35.28, 32.82, 23.10, 20.33, 19.74. APCI-MS (m/z): [M+H]+ calcd. for $C_{52}H_{41}N_4$, 721.3326; found, 721.3318; Elemental analysis calcd. (%) for $C_{52}H_{41}N_4$: C, 86.64; H, 5.59; N, 7.77; found: C, 86.61; H, 5.61; N, 7.66. T_g = 140 °C. T_m = 249 °C.

TpPXT-tFFO

Material Characterization

^{1}H NMR (800 MHz, $CDCl_3$, 300 K, δ): 8.70−8.69 (m, 4H), 8.17 (dd, J = 7.8, 1.2 Hz, 1H), 7.81 (s, 1H), 7.63−7.61 (3H) 7.56−7.54 (m, 4H), 7.51−7.50 (2H), 7.38 (d, J = 7.3 Hz 1H), 7.23−7.21 (m, 1H), 7.16 (t, J = 7.6 Hz, 1H), 7.10 (td, J = 7.2, 1.2 Hz, 1H), 7.06 (td, J = 7.2, 1.2 Hz, 1H), 6.85 (dd, 7.6, 1.0 Hz, 1H), 6.53−6.51 (m, 1H), 6.41 (ddd, J = 7.8, 7.3, 1.4 Hz, 1H), 6.14 (dd, J = 7.7, 1.4 Hz, 1H), 6.09 (dd, J = 7.7, 1.4 Hz, 1H), 5.92 (ddd, J = 7.7, 7.3, 1.4 Hz, 1H), 5.84 (ddd, J = 7.7, 7.3, 1.4 Hz, 1H), 5.64 (s, 1H), 5.44 (dd, J = 7.8, 1.4 Hz, 1H), 5.17 (dd, J = 7.8, 1.4 Hz, 1H). ^{13}C NMR (201 MHz, $CDCl_3$, 300 K, δ): 172.84, 171.29, 149.45, 147.08, 145.69, 145.48, 144.96, 143.63, 143.42, 142.93, 136.52, 133.80, 133.65, 133.50, 132.70, 132.09, 128.88, 128.87 128.65, 127.92, 127.61, 127.37, 126.84, 125.44, 125.29, 125.25, 123.78, 123.55, 123.05, 123.00, 120.95, 120.72, 115.63, 115.08, 113.19, 112.08, 54.59, 45.27. APCI-MS (m/z): [M+H]+ calcd. for $C_{47}H_{31}N_4O$, 667.2492; found, 667.2465; Elemental analysis calcd. (%) for $C_{47}H_{30}N_4O$: C, 84.66; H, 4.54; N, 8.40; O, 2.40; found: C, 84.43; H, 4.52; N, 8.34; O, 2.34. T_g = 130 °C. T_m = 326 °C.

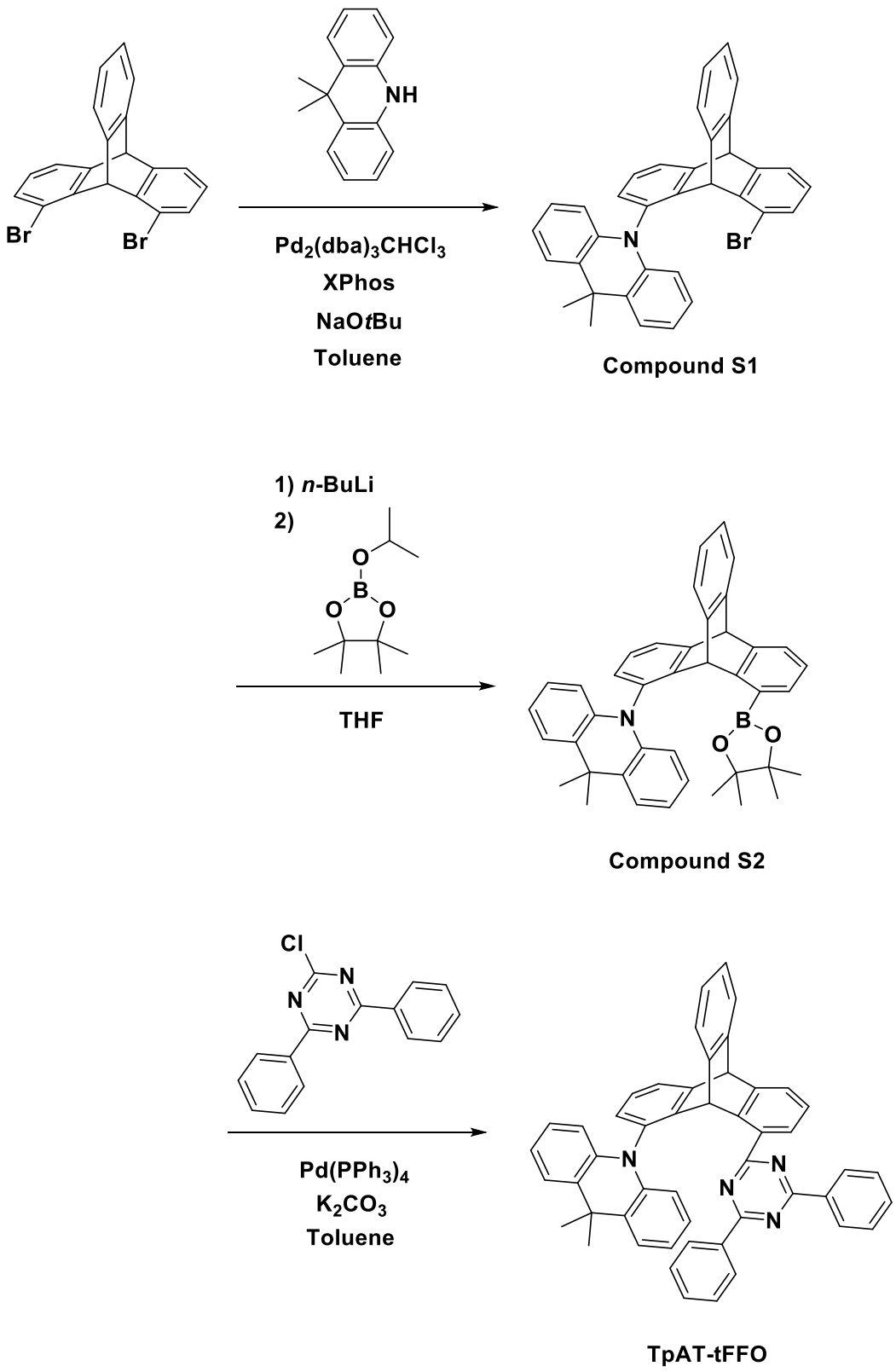

Supplementary Scheme 1 | Synthesis of TpAT-tFFO.

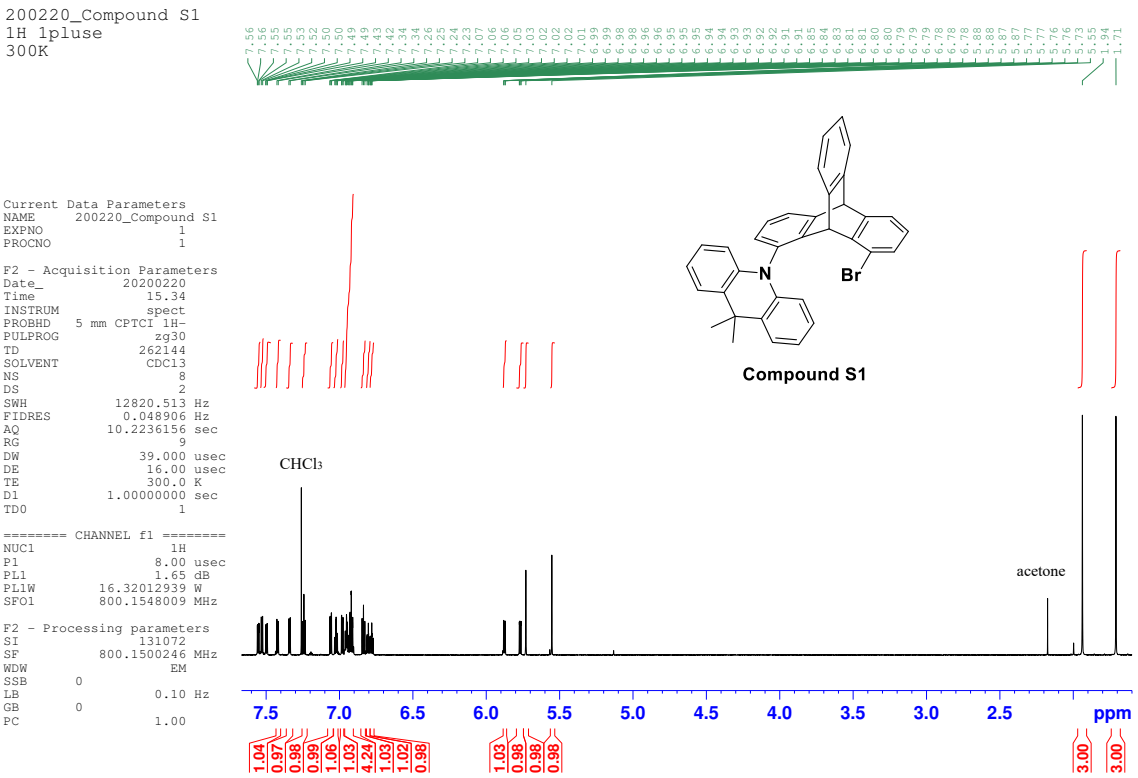

^{1}H NMR spectrum of Compound S1 measured at 300 K.

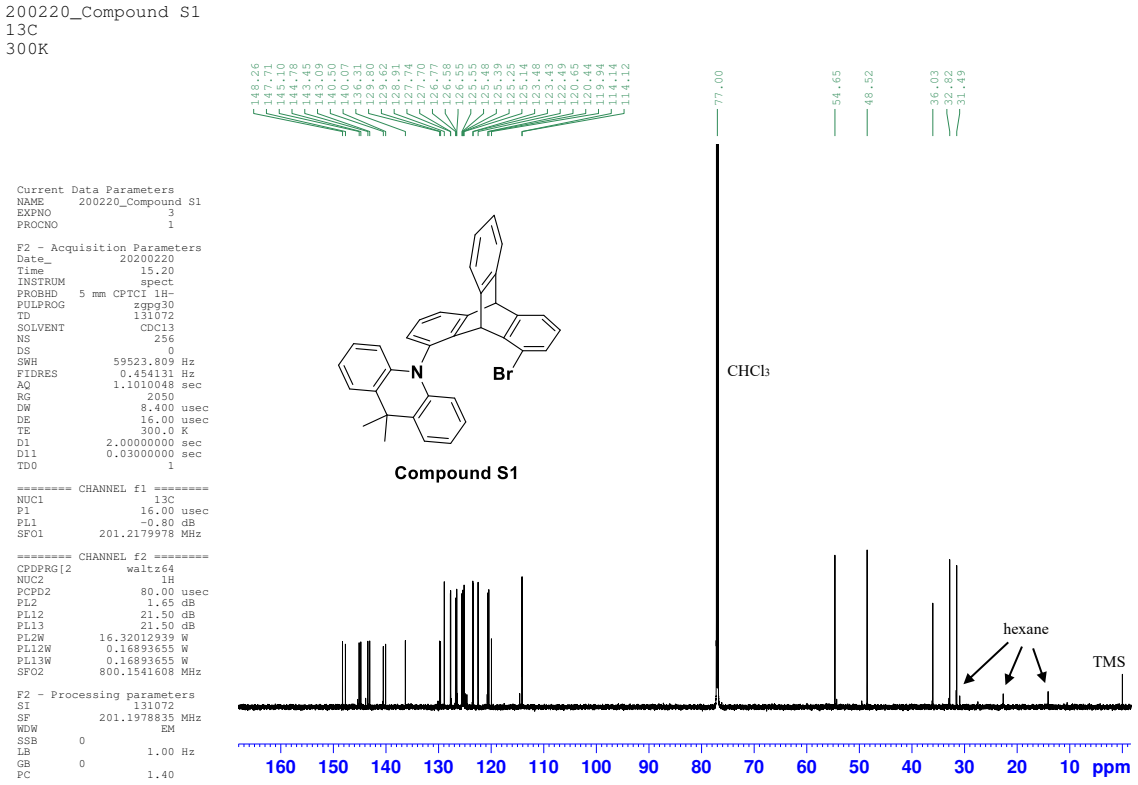

^{13}C NMR spectrum of Compound S1 measured at 300 K.

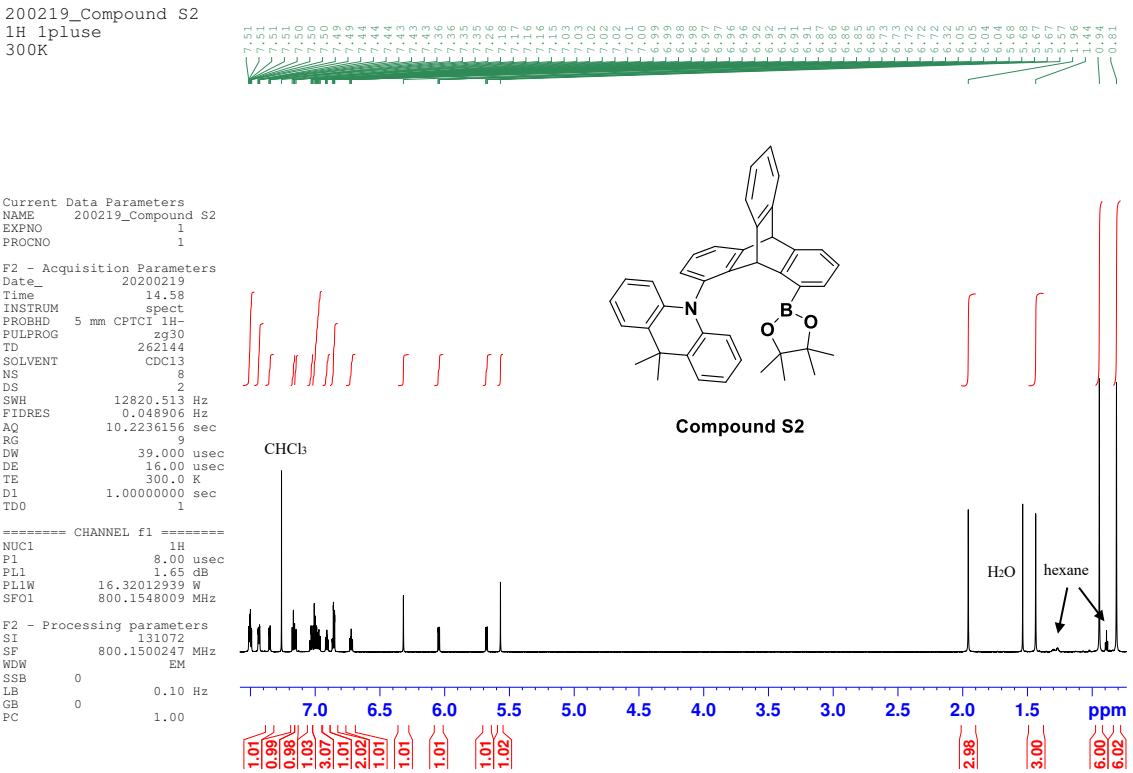

^{1}H NMR spectrum of Compound S2 measured at 300 K.

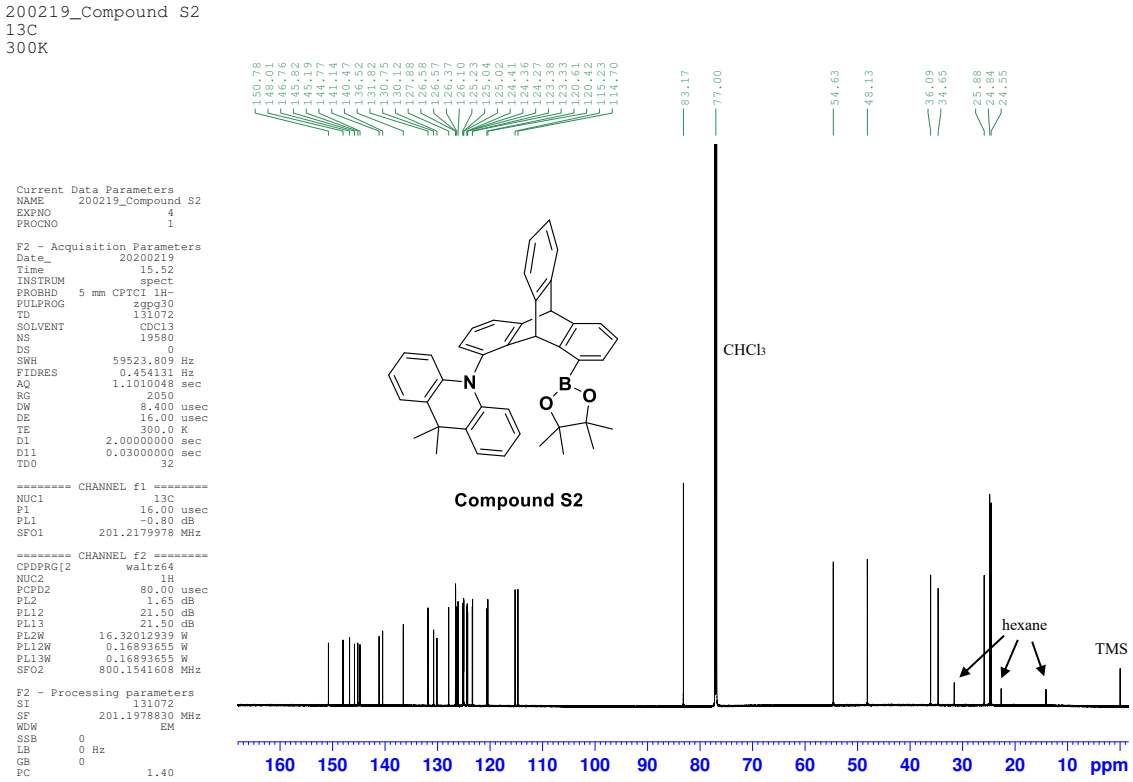

^{13}C NMR spectrum of Compound S2 measured at 300 K.

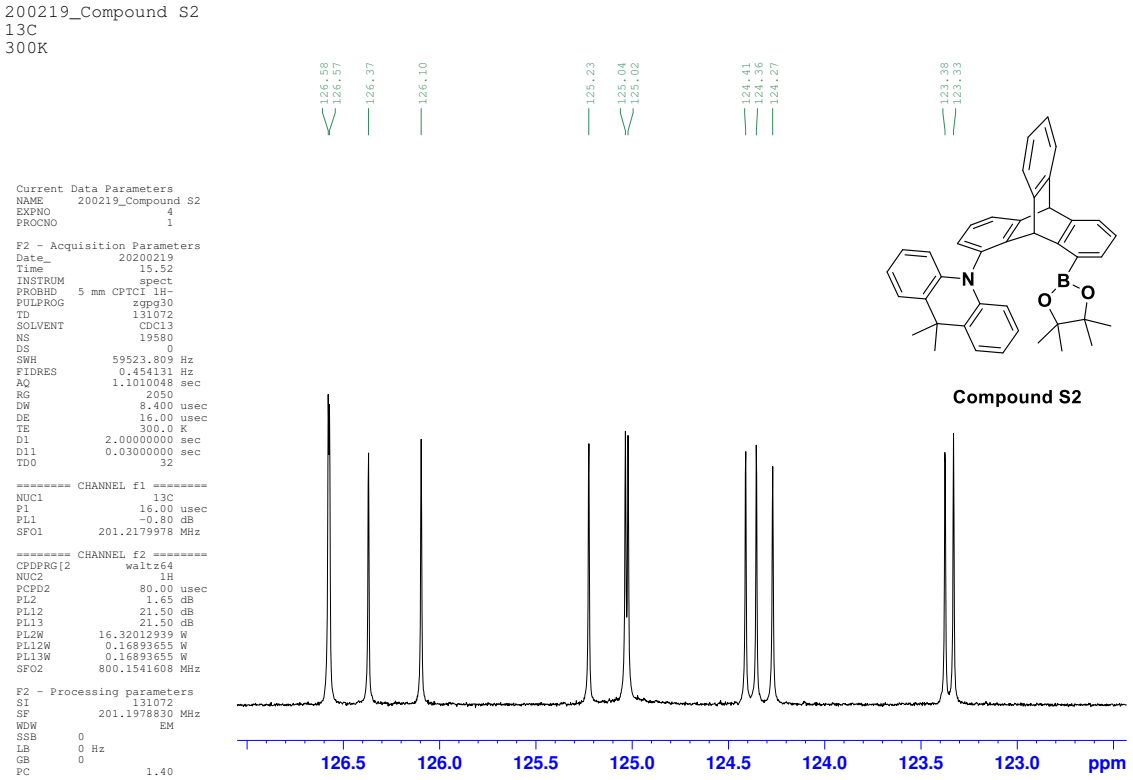

Enlarged ^{13}C NMR spectrum of Compound S2 measured at 300 K.

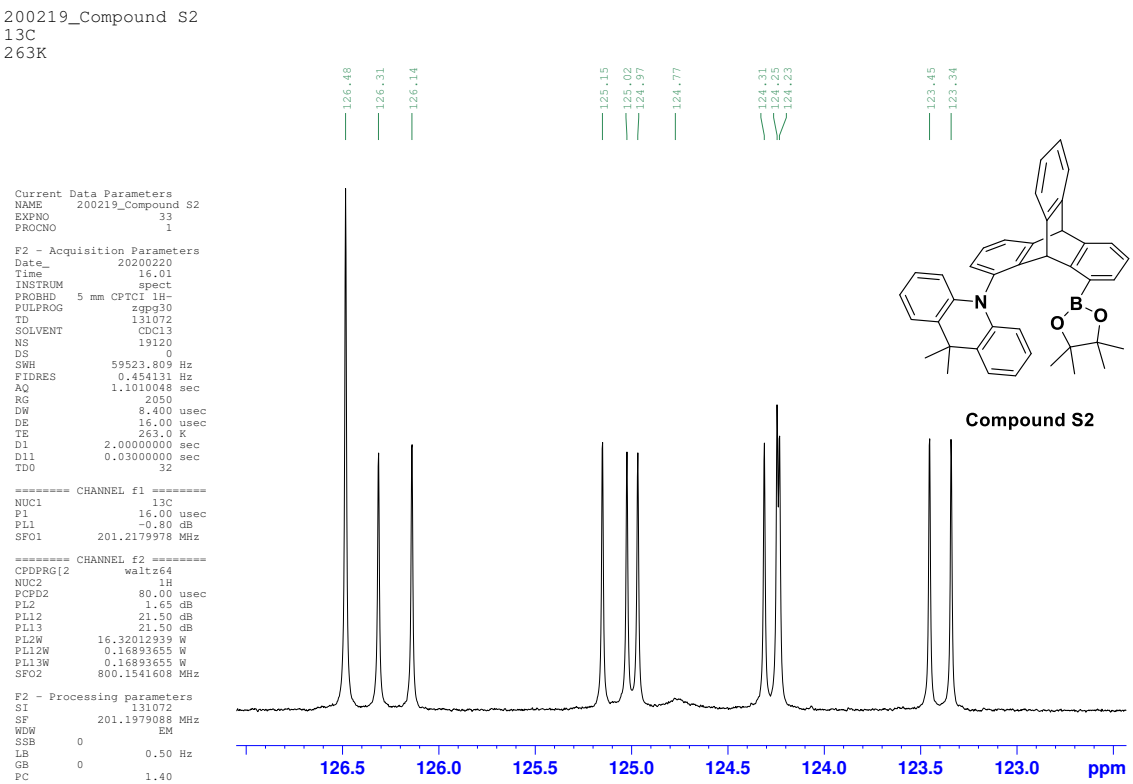

Enlarged ^{13}C NMR spectrum of Compound S2 measured at 263 K.

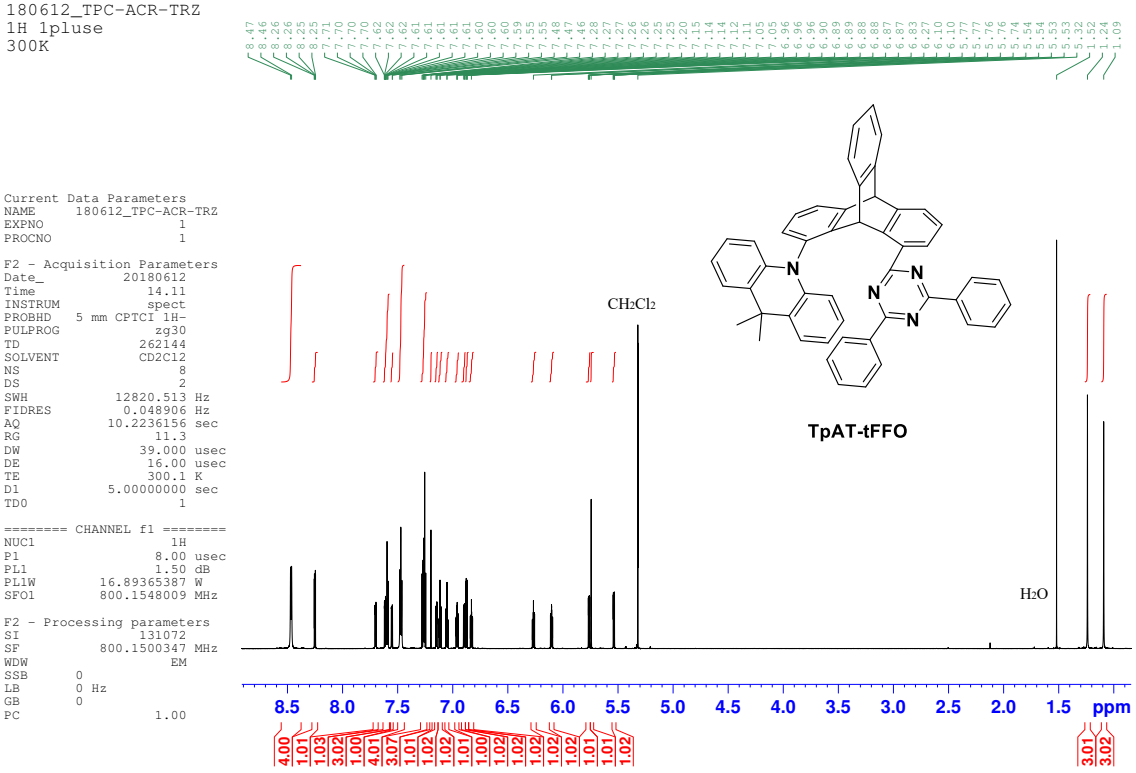

^{1}H NMR spectrum of TpAT-tFFO measured at 300 K.

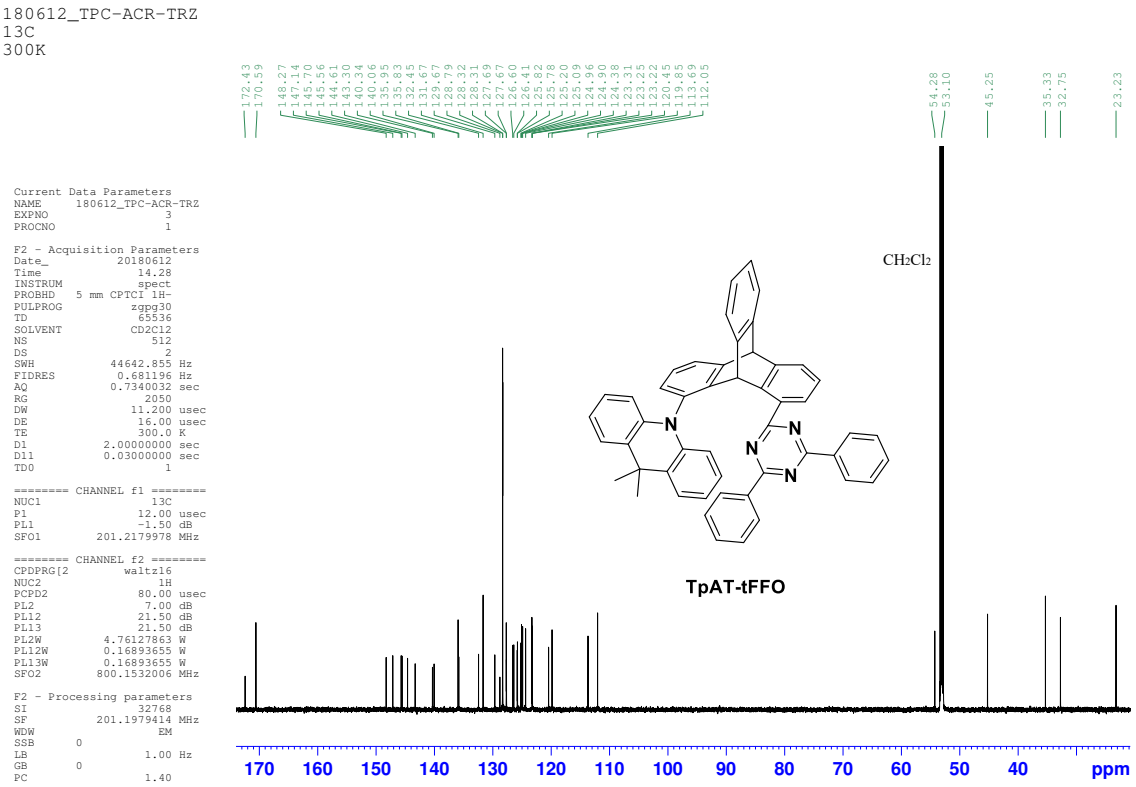

^{13}C NMR spectrum of TpAT-tFFO measured at 300 K.

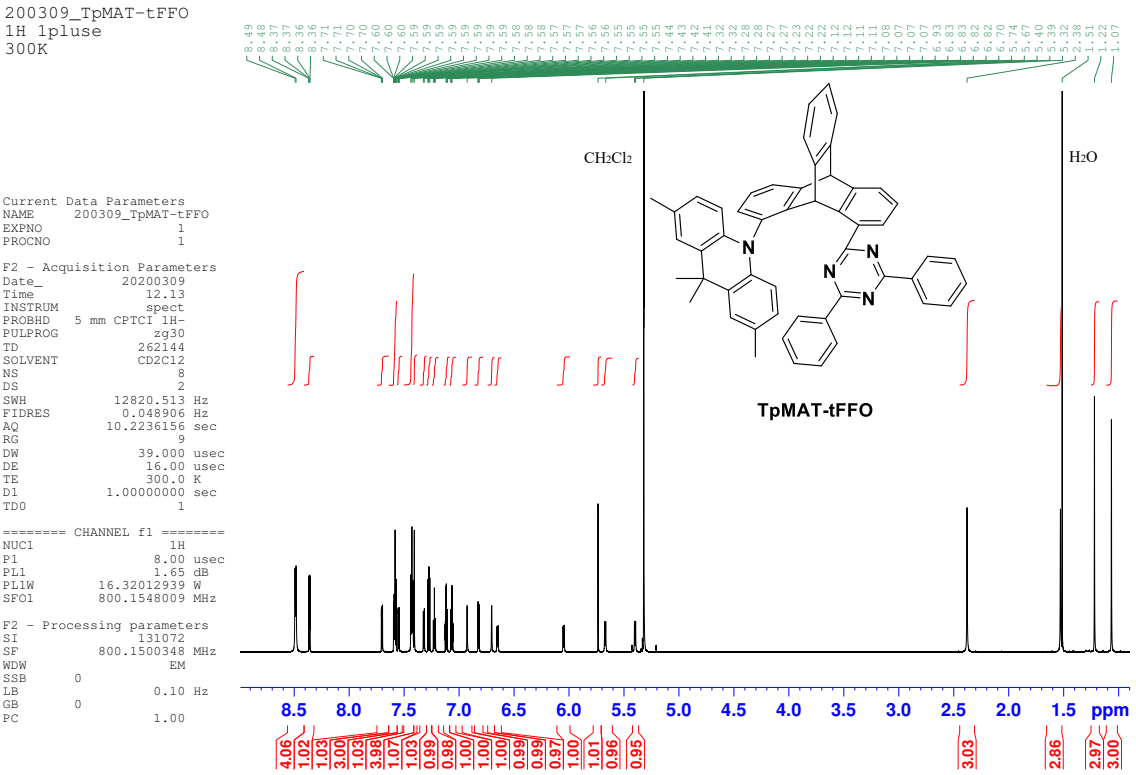


```
Current Data Parameters
NAME      200309_TpMAT-tFFO
EXPNO                    1
PROCNO                   1

F2 - Acquisition Parameters
Date_           20200309
Time              12.13
INSTRUM           spect
PROBHD   5 mm CPTCI 1H-
PULPROG           zg30
TD              262144
SOLVENT         CD2Cl2
NS                   8
DS                   2
SWH           12820.513 Hz
FIDRES         0.048906 Hz
AQ            10.2236156 sec
RG                   9
DW               39.000 usec
DE               16.00 usec
TE               300.0 K
D1            1.00000000 sec
TD0                  1

======== CHANNEL f1 ========
NUC1                1H
P1                8.00 usec
PL1               1.65 dB
PL1W        16.32012939 W
SFO1        800.1548009 MHz

F2 - Processing parameters
SI                131072
SF          800.1500348 MHz
WDW                 EM
SSB       0
LB                0.10 Hz
GB        0
PC                1.00
```

^{1}H NMR spectrum of TpMAT-tFFO measured at 300 K.

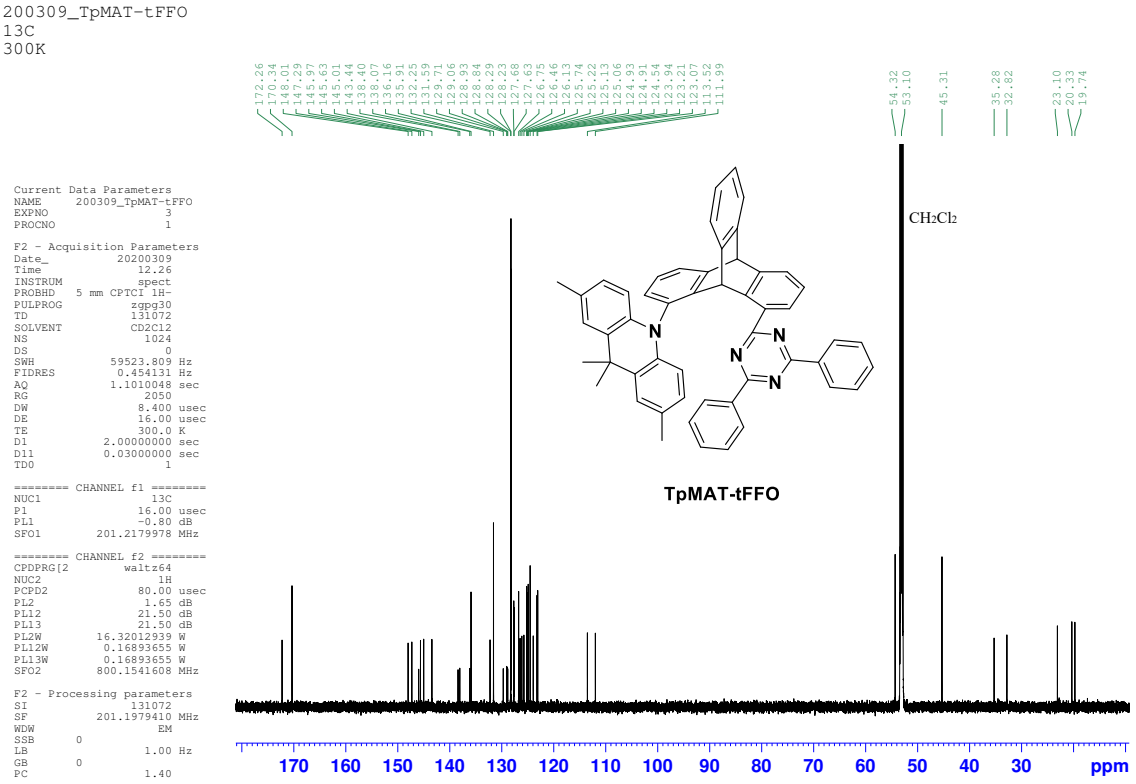


```
Current Data Parameters
NAME      200309_TpMAT-tFFO
EXPNO                    3
PROCNO                   1

F2 - Acquisition Parameters
Date_           20200309
Time              12.26
INSTRUM           spect
PROBHD   5 mm CPTCI 1H-
PULPROG         zgpg30
TD              131072
SOLVENT         CD2Cl2
NS                1024
DS                   0
SWH           59523.809 Hz
FIDRES         0.454131 Hz
AQ            1.1010048 sec
RG                2050
DW               8.400 usec
DE               16.00 usec
TE               300.0 K
D1            2.00000000 sec
D11           0.03000000 sec
TD0                  1

======== CHANNEL f1 ========
NUC1                13C
P1                16.00 usec
PL1               -0.80 dB
SFO1        201.2179978 MHz

======== CHANNEL f2 ========
CPDPRG[2          waltz64
NUC2                1H
PCPD2             80.00 usec
PL2                1.65 dB
PL12              21.50 dB
PL13              21.50 dB
PL2W        16.32012939 W
PL12W        0.16893655 W
PL13W        0.16893655 W
SFO2        800.1541608 MHz

F2 - Processing parameters
SI                131072
SF          201.1979410 MHz
WDW                 EM
SSB       0
LB                1.00 Hz
GB        0
PC                1.40
```

^{13}C NMR spectrum of TpMAT-tFFO measured at 300 K.

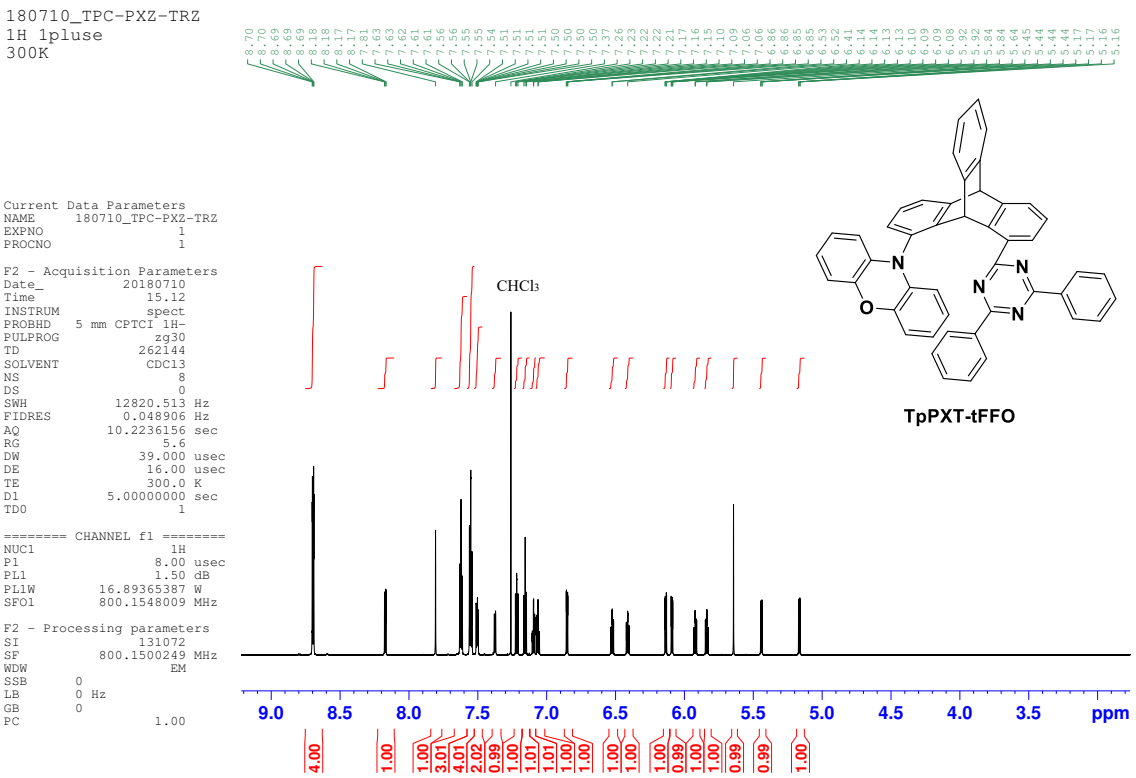

^{1}H NMR spectrum of TpPXT-tFFO measured at 300 K.

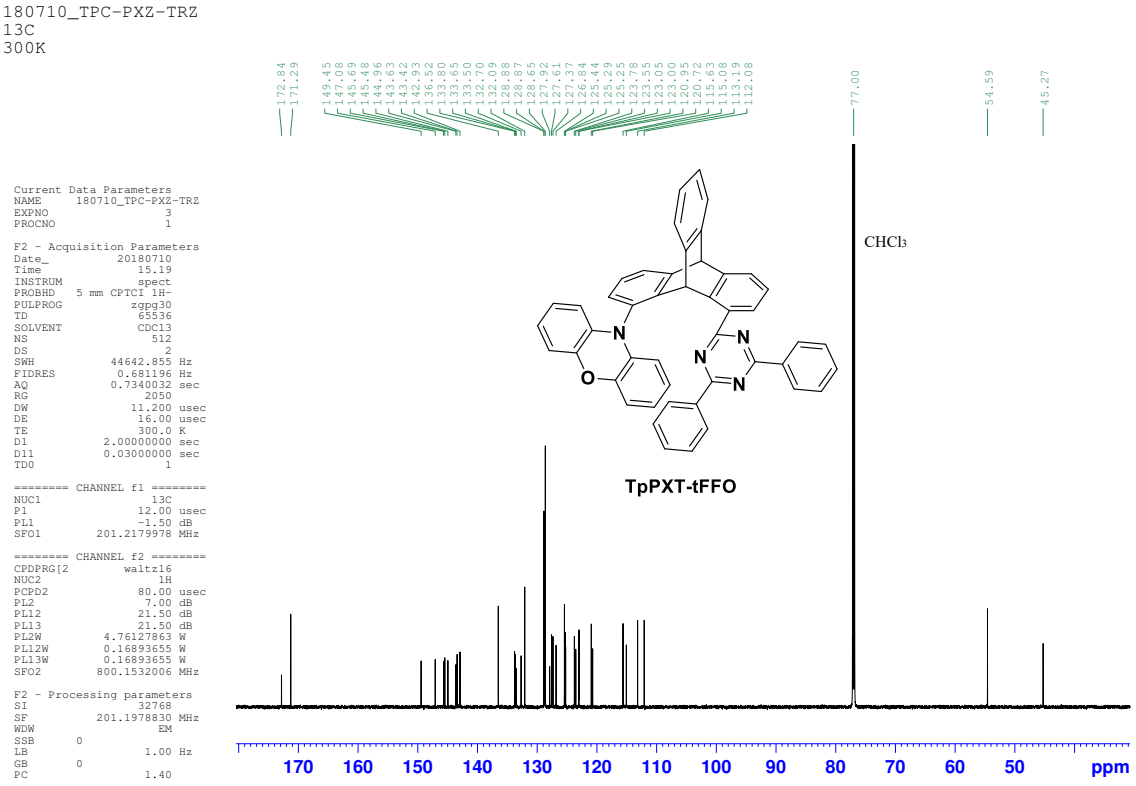

^{13}C NMR spectrum of TpPXT-tFFO measured at 300 K.

Theoretical calculations

Optimization of parameters, ω for LC-ωPBE functional and γ for LCY-ωPBE functional

Optimization of the range-separation parameter, ω, for LC-ωPBE functional was performed according to ref. S2. As shown in Supplementary Fig. 1a, the optimal value of ω was determined from the point exhibiting minimum J^2, where $J^2 = \sum_{i=0}^{1}[\varepsilon_H(N+i) + IP(N+i)]^2$. Here, N, $\varepsilon_H(N)$, and $IP(N)$ denote the electron number of the target molecule, its HOMO energy, and vertical ionization potential, respectively. Optimization of the range parameter γ for LCY-ωPBE functional was performed by the same procedure and the results are summarized in Supplementary Fig. 7.

Thermal and photophysical properties

General procedure for thermal measurements

Glass transition temperatures (T_g) were determined from the onset of the differential scanning calorimetry (DSC) curve of the 2nd heating scan using a DSC1 (METTLER TOLEDO) at a heating rate of 10 °C min^{-1}. The 1st heating scan was performed to 300 °C, which is approximately 40 °C higher than the melting point of the powder sample and the melted sample was quenched rapidly on an Al plate to form an amorphous sample.

General procedure for photophysical measurements

UV-vis absorption spectra and photoluminescence (PL) spectra were measured by a UV-vis spectrophotometer (V-750ST, JASCO, Japan) and a spectrofluorometer (FluoroMax Plus, HORIBA, Japan), respectively. Photoluminescence quantum yield (PLQY or Φ_{PL}) was measured with an absolute PLQY spectrometer (C9920-02, Hamamatsu Photonics, Japan). The PLQY values in 10^{-4} M toluene solution were collected with and without 30 min of Ar gas bubbling with an excitation wavelength of 365 nm. Here we used a toluene solvent of spectrochemical analysis grade purchased from FUJIFILM Wako Pure Chemical Corporation. The PLQYs for films were measured under a N_2 flow. The temperature-dependent transient PL decay measurements were conducted with a fluorescence lifetime measurement system (Quantaurus-Tau C11367-01, Hamamatsu Photonics, Japan) equipped with a cryostat (Oxford Instruments, Optistat DN2, UK).

Results

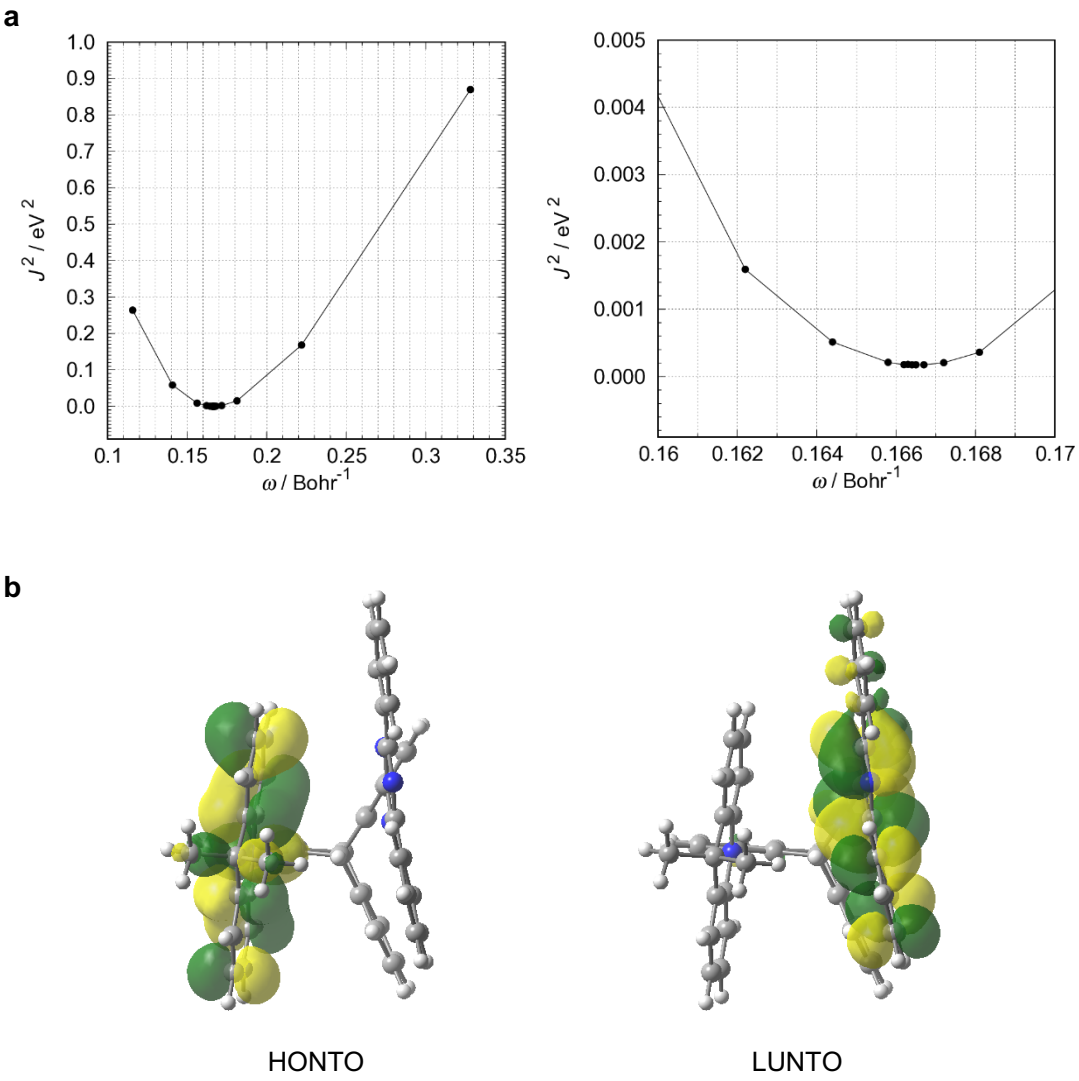

Supplementary Figure 1 | Theoretical calculation of TpAT-tFFO. a, J^2-ω plot of TpAT-tFFO for LC-ωPBE functional with 6-31+G(d) basis set. The minimum region of the left figure is enlarged in the right. **b,** Natural transition orbitals (NTO) of S_1 state of TpAT-tFFO. The spatial distributions of the highest occupied NTO (HONTO) and lowest unoccupied NTO (LUNTO) indicate a through-space interaction of the donor and acceptor.

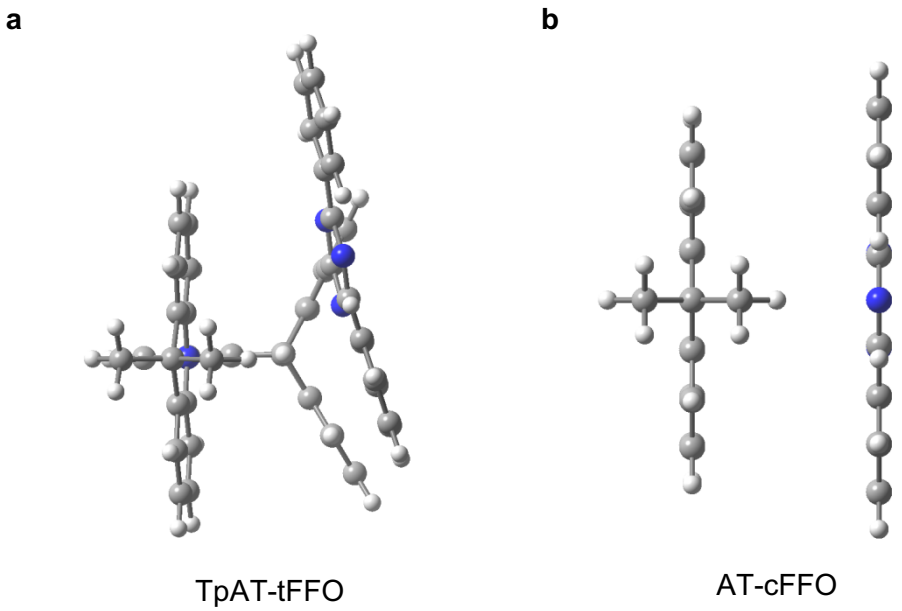

Supplementary Figure 2 | Geometric structures. a, TpAT-tFFO and **b**, AT-cFFO (in **b**, π-planes of A and T segments are in a completely parallel alignment with d_{DA} of 4.72 Å).

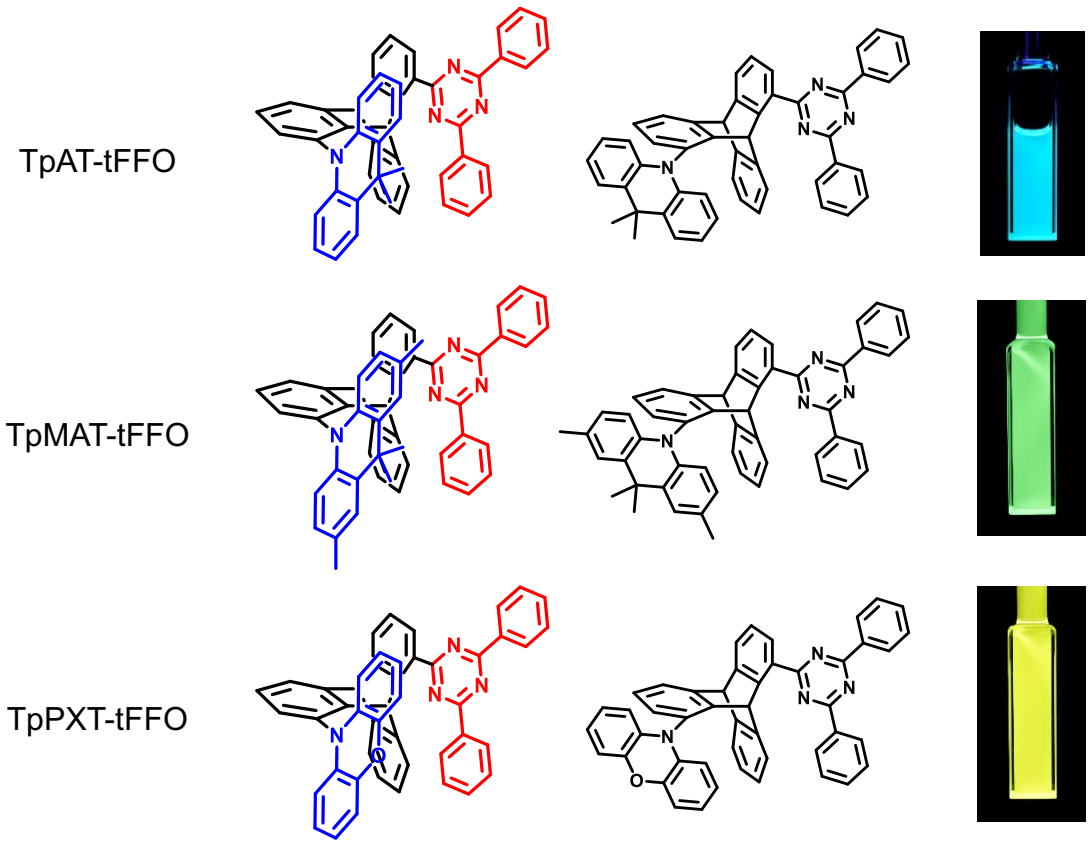

Supplementary Figure 3 | Chemical structures and emission colours of TpAT-tFFO, TpMAT-tFFO, and TpPXT-tFFO. DFT-optimized structures are shown in the left. In the middle, schematic structures clearly show the donor segments. Photographs on the right show their toluene solutions under UV-light irradiation.

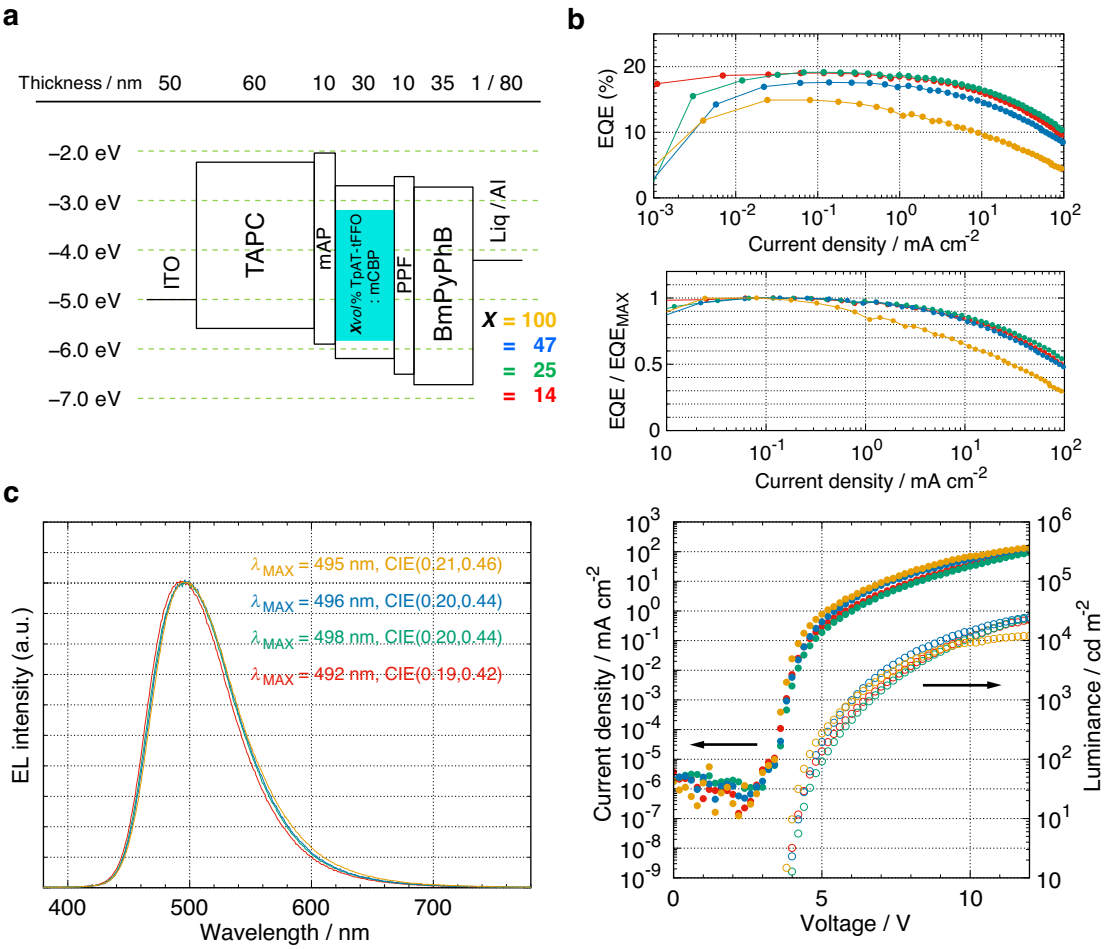

Supplementary Figure 4 | TpAT-tFFO based TADF-OLEDs. a, Device structure of the OLEDs. **b**, Device performances of EQE-luminance (top), normalized EQE-current density (middle), and current density-voltage-luminance characteristics (bottom). Normalized EQE is EQE/EQE_{MAX}. **c,** EL spectra of the OLEDs at 10 mA cm^{-2}. Results of OLEDs with doping concentrations of 14, 25, 47 and 100 vol% are represented by red, green, blue and yellow, respectively.

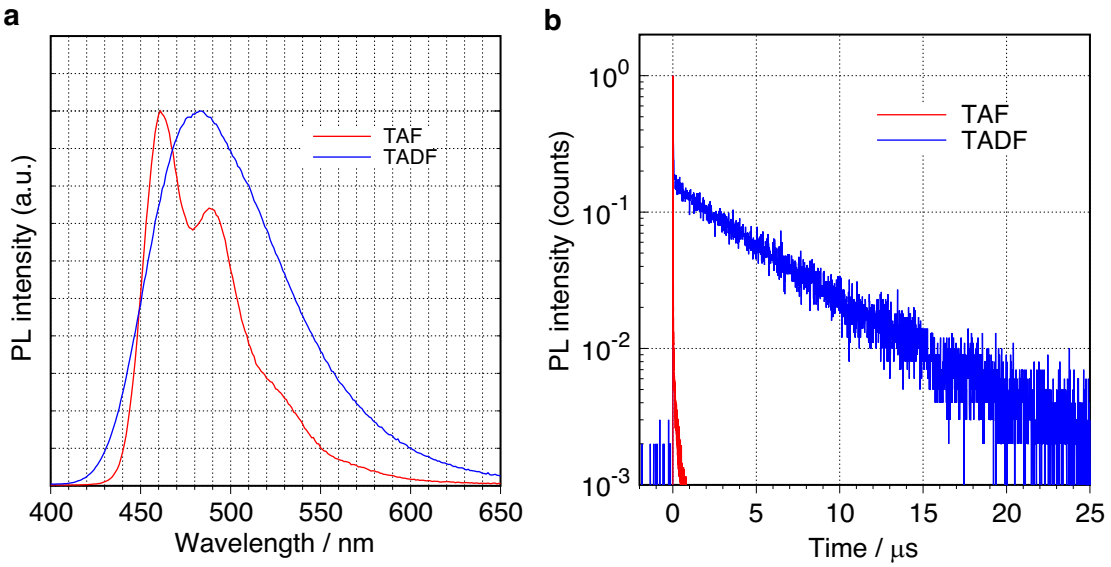

Supplementary Figure 5 | Photophysical property. a, PL spectra and **b,** transient PL decay curves of 4 vol%TBPe:26 vol%TpAT-tFFO:CzSi film (TAF) and 25 vol%TpAT-tFFO:CzSi film (TADF). PL intensities of the transient PL decay curves were monitored at 460 and 478 nm, respectively.

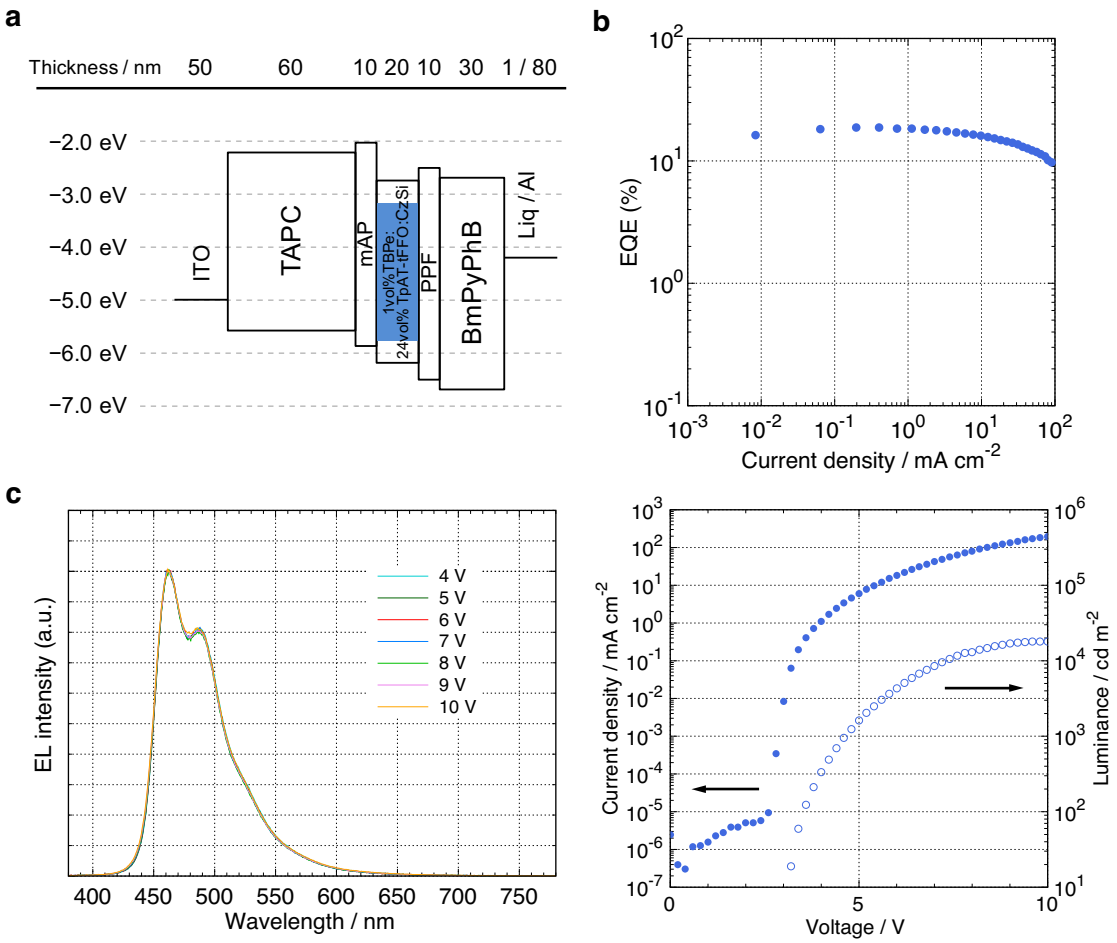

Supplementary Figure 6 | TpAT-tFFO based TAF-OLED using 1 vol%TBPe:24 vol%TpAT-tFFO:CzSi as emitting layer. a, Device structure of the TAF-OLED. **b,** Device performances of EQE-current density (top) and current density-voltage-luminance characteristics (bottom). **c,** EL spectra of the TAF-OLEDs at different voltages.

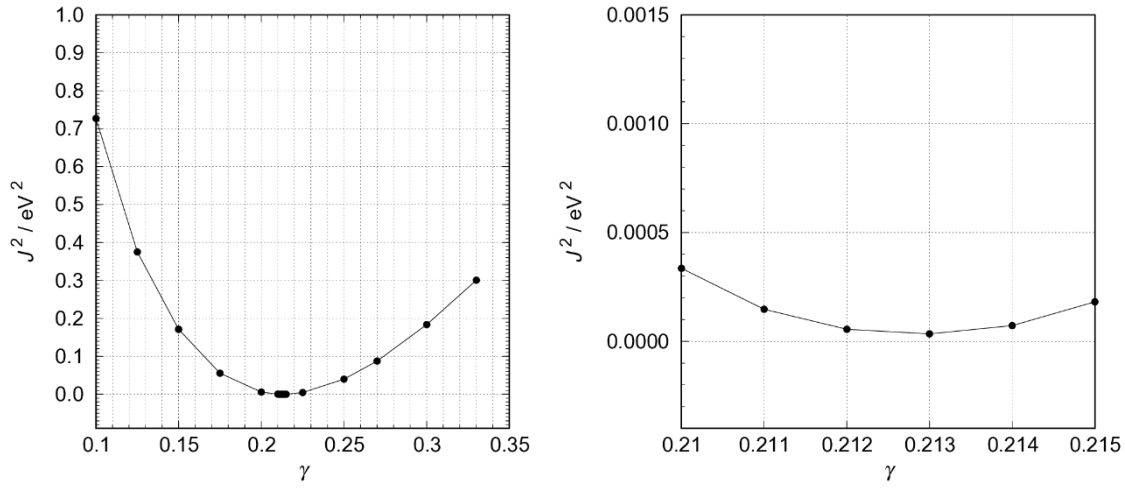

Supplementary Figure 7 | J^2-γ plot of TpAT-tFFO for LCY-ωPBE functional with TZP basis set. Region near the minimum J^2 in the left figure is enlarged on the right.

Supplementary Table 1 | Results of TD-DFT calculation of TpAT-tFFO (LC-ωPBE functional with 6-31+G(d) basis set with the optimal ω of 0.1664 Bohr^{-1}).

HOMO / eV	LUMO / eV	T_1 / eV	S_1 / eV	ΔE_{ST} / eV	$f(S_0 \rightarrow S_1)$	$\Delta E(^3CT \rightarrow ^3LE)$ / eV	$\Delta E(^3LE \rightarrow ^1CT)$ / eV
−6.47	−0.90	3.10	3.12	0.0186	0.0004	0.0751	−0.0565

Supplementary Table 2 | Fitting data for transient PL decay curves and PLQYs of the 10^{-4} M toluene solution of TpAT-tFFO without and with 30-min Ar gas bubbling. PL decay curves were fitted by the equation, $[\text{PL intensity}] = A_p \exp\left(-\frac{t}{\tau_p}\right) + A_d \exp\left(-\frac{t}{\tau_d}\right)$. Here, A and τ denote the prefactor and lifetime, respectively. Subscripts p and d correspond to prompt and delayed components, respectively. Φ_{total}, Φ_p and Φ_d denote the PLQY of total, prompt and delayed components, respectively.

Ar bubbling	τ_p / ns	τ_d / μs	A_p	A_d	Φ_{total} (%)	Φ_p (%)	Φ_d (%)
Without (w/o)	9.93	—	78.3	—	1.8	1.8 (100%)[a]	—
With (w/)	15.3	4.42	60.2	8.70	84	2.0 (2.33%)	82.0 (97.7%)

[a]Percentages in relation to the total PLQY was shown in parentheses.

Supplementary Table 3 | Values of rate constants, k_r^S, k_{nr}^S, k_{ISC}, and k_{RISC}, of tFFO-based TADF emitters in this study. The experimentally-obtained values necessary for the analysis of these rate constants are also provided.

Emitter	k_p / s^{-1}	k_d / s^{-1}	Φ_p (%)	Φ_d (%)	k_r^S / s^{-1}	k_{nr}^S / s^{-1}	k_{ISC} / s^{-1}	k_{RISC} / s^{-1}
TpAT-tFFO	6.6×10^7	2.3×10^5	2.0	82.0	1.1×10^6	2.0×10^5	5.3×10^7	1.2×10^7
TpMAT-tFFO	4.8×10^7	3.5×10^5	3.1	64.9	1.2×10^6	5.8×10^5	3.7×10^7	9.2×10^6
TpPXT-tFFO	6.2×10^7	3.3×10^5	2.0	25.0	1.2×10^6	3.1×10^6	5.3×10^7	4.8×10^6

Supplementary Table 4 | Summary of the organic materials with $k_{RISC} \geq 10^6\ s^{-1}$. Data are collected from journal articles where the respective materials were first reported. Previously reported materials composed only of H, C, and N are highlighted in sky-blue. Those of H, C, N and O are highlighted in pink. Inclusion of sulphur (highlighted in pale green) in our tFFO-based materials will provide much larger k_{RISC} values.

Emitter	Composed of	k_{RISC} ($\times 10^6\ s^{-1}$)	References
TpAT-tFFO	H, C, N	**12**	**This work**
TpMAT-tFFO	H, C, N	**9.2**	
TpPXT-tFFO	H, C, N, **O**	**4.8**	
Ac3TRZ3	H, C, N	1.0	Wang *et al.*, *Chem. Sci.* (2019)[S3]
TAc3TRZ3	H, C, N	2.1	
2Cz3DPhCzBN	H, C, N	1.0	Noda *et al.*, *Sci. Adv.* (2018)[S4]
PCzATD5	H, C, N	2.0	Wang *et al.*, *J. Mater. Chem. C* (2018)[S5]
DTRZ-DI	H, C, N	1.6	Kim *et al.*, *J. Mater. Chem. C* (2018)[S6]
TRZ-DI	H, C, N	1.6	
4CzIPN	H, C, N	~1.3	Uoyama *et al.*, *Nature* (2012)[S7]
TRZ-m-ACRSA	H, C, N, **O**	1.2	Gan *et al.*, *Adv. Funct. Mater.* (2019)[S8]
DMF-BP-PXZ	H, C, N, **O**	1.0	Guo *et al.*, *Adv. Sci.* (2019)[S9]
DPF-BP-PXZ	H, C, N, **O**	1.2	
SBF-BP-PXZ	H, C, N, **O**	1.1	
DPxBn	H, C, N, **O**	1.6	Kim *et al.*, *J. Phys. Chem. C* (2018)[S10]
MCz-XT	H, C, N, **O**	~ 2	Lee *et al.*, *Adv. Mater.* (2017)[S11]
DC-ACR	H, C, N, **O**	2.6	Chen *et al.*, *J. Mater. Chem. C* (2017)[S12]
BTH-DMF	H, C, N, **S**	2.8	Liu *et al.*, *Adv. Opt. Mater.* (2018)[S13]
TDBA-DI	H, C, N, **B, O**	1.1	Ahn *et al.*, *Nat. Photon.* (2019)[S14]
MPAc-BO	H, C, N, **B, O**	1.0	Park *et al.*, *Adv. Funct. Mater.* (2018)[S15]
TB-3PXZ	H, C, N, **B, O**	1.9	Liu *et al.*, *J. Mater. Chem. C* (2016)[S16]
2	H, C, N, **B, S**	3.2	Matsuo and Yasuda, *Chem. Commun.* (2019)[S17]
MPAc-BS	H, C, N, **B, S**	3.5	Park *et al.*, *Adv. Funct. Mater.* (2018)[S15]
TAT-3DBTO$_2$ [a]	H, C, N, **O, S**	0.092–15[a]	dos Santos *et al.*, *Adv. Sci.* (2018)[S18]
Cop-50	H, C, N, **O, S**	2.6	Liu *et al.*, *Macromolecules* (2018)[S19]
Cop-10	H, C, N, **O, S**	1.4	
DPTZ-DBTO$_2$	H, C, N, **O, S**	1.9 ± 0.1	Dias *et al.*, *Adv. Sci.* (2016)[S20]
BrPPM	H, C, N, **O, Br**	1.0	Xiang *et al.*, *J. Mater. Chem. C* (2017)[S21]
2F-BTH-DMF	H, C, N, **F, S**	2.4	Liu *et al.*, *Adv. Opt. Mater.* (2018)[S13]
MFAc-SPS	H, C, N, **P, S**	1.9	Lee *et al.*, *J. Mater. Chem. C* (2018)[S22]
PTZ-mPYRCl	H, C, N, **S, Cl**	2.0	Serevicius *et al.*, *Chem. Commun.* (2019)[S23]
MFAc-SPO	H, C, N, **O, P, S**	1.1	Lee *et al.*, *J. Mater. Chem. C* (2018)[S22]

All the values in this table are rounded to no more than two significant figures.

[a] For TAT-3DBTO$_2$, k_{RISC} values are displayed as a range because the delayed fluorescence was fitted with three exponential curves, resulting in three k_{RISC} values of different orders. The k_{RISC} values were widely distributed over more than two orders of magnitude and the average value is much smaller than the highest value.

Supplementary Table 5 | Device performances of TpAT-tFFO-based OLEDs with doping concentration of 25 vol% w/ and w/o out-coupling sheet.

Emitter	EQE_{MAX}	EQE_{100}[a]	$EQE_{1,000}$	$EQE_{10,000}$	$EQE_{20,000}$	L_{MAX} / cd m^{-2}	CIE(x,y)[c]
TpAT-tFFO (w/ oc sheet)	29.0	29.0 (0.3%)[b]	27.6 (4.8%)	22.8 (21.4%)	19.7 (32.1%)	48,930	(0.20, 0.41)
TpAT-tFFO (w/o oc sheet)	19.2	19.1 (0.4%)	18.1 (5.4%)	14.4 (24.7%)	11.6 % (38.9%)	33,870	(0.20, 0.44)

(a) EQE_Y denotes EQE value at Y = cd m^{-2}.

(b) EQE roll-off (%) was shown in parentheses, where EQE roll-off (%) = (EQE_{MAX}−EQE) / EQE_{MAX} × 100.

(c) Colour coordinates of Commission Internationale de l'Eclairage (CIE).

Supplementary Table 6 | Device performance of OLEDs with different doping concentrations, *X* (vol%). The device structures are ITO (50 nm)/TAPC (60 nm)/mAP (10 nm)/*X* vol% TpAT-tFFO:mCBP (30 nm)/PPF (10 nm)/BmPyPhB (35 nm)/Liq (1 nm)/Al (80 nm).

dopant conc. ***X*** (vol%)	EQE_{MAX}	EQE_{1000}	$EQE_{10,000}$	$EQE_{20,000}$
14	19.0	17.8	13.3	9.9
25	**19.2**	**18.1**	**14.4**	**11.7**
47	17.6	16.3	11.7	8.8
100	14.9	11.4	4.7	—

Supplementary Table 7 | Device performances of TpAT-tFFO-based TAF-OLEDs. Preceding performances of TAF-OLEDs s using TBPe as an emitter are also shown for comparison.

Emitting layer	EQE (%)				CIE(*x*,*y*)	References
	EQE_{MAX}	$EQE_{1,000}$[a]	$EQE_{5,000}$	$EQE_{10,000}$		
1vol%TBPe:24vol% TpAT-tFFO:CzSi	**18.7**	**17.1**	**14.4**	**11.8**	**(0.15, 0.23)**	**This work**
1wt%TBPe:15wt% ACRSA:DPEPO	13.4	8.7	N.A.	—	(0.17, 0.30)	Ref. S24
0.1wt%TBPe:50wt% CzAcSF:DPEPO	18.1	N.A.[b]	N.A.	—	(0.15, 0.22)	Ref. S25
TBPe:CzAcSF:DPEPO	18	N.A.	N.A.	N.A.	N.A.	Ref. S26
TBPe:DMAC-DPS:DPEPO	18.8	13.5	N.A.	—	(0.14, 0.25)	Ref. S27
0.5wt%TBPe:5CzCN :DPOBBPE	19.5	N.A.	—[c]	—	(0.15, 0.23)	Ref. S28

(a) EQE_Y denotes EQE value at Y cd m^{-2}.

(b) N.A. denotes that data was not assigned.

(c) — denotes that the device do not reach the luminance.

Perspective

Our main purpose here is to demonstrate the effectiveness of our molecular design focusing on enhancement of RISC processes. The Tp scaffold provides an optimal d_{DA} to realize $E(^1CT) \approx E(^3CT) \approx E(^3LE)$ and considerable SOCMEV. The experimentally-obtained very large k_{RISC} values for the three tFFO molecules substantiate the validity of our tFFO concept. In contrast, the radiative decay is relatively slow despite the large PLQY. However, the process can be expedited within our tFFO-design. Tp with donor and acceptor moieties at the 1st and 8th positions provides a relatively large d_{DA} of 4.72 Å resulting in small *f*-value. However, as shown in Figure 1b, we can increase the *f*-value by simply reducing d_{DA}. For example, at d_{DA} = 3.5 Å, the *f*-value can be increased to be an order of magnitude greater, while ΔE_{ST} remains sufficiently small, < 0.1 eV. Energy level matching between CT and LE can be also tuned. This result indicates that it is possible to improve fluorescence decay processes by reducing d_{DA} without sacrificing any other properties. We are now trying to develop such new tFFO-based materials based on different scaffolds.

References

S1. Grossman, O. & Gelman, D. Novel trans-spanned palladium complexes as efficient catalysts in mild and amine-free cyanation of aryl bromides under air. *Org. Lett.* **8**, 1189–1191 (2006).

S2. Sun, H., Zhong, C. & Brédas, J.-L. Reliable prediction with tuned range-separated functionals of the singlet-triplet gap in organic emitters for thermally activated delayed fluorescence. *J. Chem. Theory. Comput.* **11**, 3851–3858 (2015).

S3. Wang, X., *et al.* Through-space charge transfer hexaarylbenzene dendrimers with thermally activated delayed fluorescence and aggregation-induced emission for efficient solution-processed OLEDs. *Chem. Sci.* **10**, 2915–2923 (2019).

S4. Noda, H., Nakanotani, H. & Adachi, C. Excited state engineering for efficient reverse intersystem crossing. *Sci. Adv.* **4**, eaao6910 (2018).

S5. Wang, Y., *et al.* Efficient non-doped yellow OLEDs based on thermally activated delayed fluorescence conjugated polymers with an acridine/carbazole donor backbone and triphenyltriazine acceptor pendant. *J. Mater. Chem. C* **6**, 568–574 (2018).

S6. Kim, K.J., *et al.* A new rigid diindolocarbazole donor moiety for high quantum efficiency thermally activated delayed fluorescence emitter. *J. Mater. Chem. C* **6**, 1343–1348 (2018).

S7. Uoyama, H., Goushi, K., Shizu, K., Nomura, H. & Adachi, C. Highly efficient organic light-emitting diodes from delayed fluorescence. *Nature* **492**, 234–238 (2012).

S8. Gan, L., *et al.* Utilizing a Spiro TADF Moiety as a functional electron donor in TADF molecular design toward efficient "multichannel" reverse intersystem crossing. *Adv. Funct. Mater.* **29**, 1808088 (2019).

S9. Guo, J., *et al.* Mechanical insights into aggregation-induced delayed fluorescence materials with anti-Kasha behavior. *Adv. Sci.* **6**, 1801629 (2019).

S10. Kim, H.S., *et al.* Photophysical properties of thermally activated delayed fluorescent materials upon distortion of central axis of donor moiety. *J. Phys. Chem. C* **122**, 28576–28587 (2018).

S11. Lee, J., Aizawa, N., Numata, M., Adachi, C. & Yasuda, T. Versatile molecular functionalization for inhibiting concentration quenching of thermally activated delayed fluorescence. *Adv. Mater.* **29**, 1604856 (2017).

S12. Chen, D., *et al.* Efficient solution-processed red all-fluorescent organic light-emitting diodes employing thermally activated delayed fluorescence materials as assistant hosts: molecular design strategy and exciton dynamic analysis. *J. Mater. Chem. C* **5**, 5223–5231 (2017).

S13. Liu, J., *et al.* Experimental evidence for "hot exciton" thermally activated delayed fluorescence emitters. *Adv. Opt. Mater.* **7**, 1801190 (2018).

S14. Ahn, D.H., *et al.* Highly efficient blue thermally activated delayed fluorescence emitters based on symmetrical and rigid oxygen-bridged boron acceptors. *Nat. Photon.* **13**, 540–546 (2019).

S15. Park, I.S., Matsuo, K., Aizawa, N. & Yasuda, T. High-performance dibenzoheteraborin-based thermally activated delayed fluorescence emitters: molecular architectonics for concurrently achieving narrowband emission and efficient triplet-singlet spin conversion. *Adv. Funct. Mater.* **28**, 1802031 (2018).

S16. Liu, Y., *et al.* Boosting reverse intersystem crossing by increasing donors in triarylboron/phenoxazine hybrids: TADF emitters for high-performance solution-processed OLEDs. *J. Mater. Chem. C* **4**, 4402–4407 (2016).

S17. Matsuo, K. & Yasuda, T. Boronate- and borinate-based pi-systems for blue thermally activated delayed fluorescence materials. *Chem. Commun.* **55**, 2501–2504 (2019).

S18. dos Santos, P.L., *et al.* Triazatruxene: A rigid central donor unit for a D-A_3 thermally activated delayed fluorescence material exhibiting sub-microsecond reverse intersystem crossing and unity quantum yield via multiple singlet-triplet state pairs. *Adv. Sci.* **5**, 1700989 (2018).

S19. Liu, Y., *et al.* Efficient thermally activated delayed fluorescence conjugated polymeric emitters with tunable nature of excited states regulated via carbazole derivatives for solution-processed OLEDs. *Macromolecules* **51**, 4615–4623 (2018).

S20. Dias, F.B., *et al.* The role of local triplet excited states and D-A relative orientation in thermally activated delayed fluorescence: photophysics and devices. *Adv. Sci.* **3**, 1600080 (2016).

S21. Xiang, Y., *et al.* Halogen-induced internal heavy-atom effect shortening the emissive lifetime and improving the fluorescence efficiency of thermally activated delayed fluorescence emitters. *J. Mater. Chem. C* **5**, 12204–12210 (2017).

S22. Lee, J., Aizawa, N. & Yasuda, T. Molecular engineering of phosphacycle-based thermally activated delayed fluorescence materials for deep-blue OLEDs. *J. Mater. Chem. C* **6**, 3578–3583 (2018).

S23. Serevicius, T., *et al.* Emission wavelength dependence on the rISC rate in TADF compounds with large conformational disorder. *Chem. Commun.* **55**, 1975–1978 (2019).

S24. Nakanotani, H., *et al.* High-efficiency organic light-emitting diodes with fluorescent emitters. *Nat. Commun.* **5**, 4016 (2014).

S25. Lee, I.H., Song, W., Lee, J.Y. & Hwang, S.-H. High efficiency blue fluorescent organic light-emitting diodes using a conventional blue fluorescent emitter. *J. Mater. Chem. C* **3**, 8834–8838 (2015).

S26. Song, W., Lee, I. & Lee, J.Y. Host engineering for high quantum efficiency blue and white fluorescent organic light-emitting diodes. *Adv. Mater.* **27**, 4358–4363 (2015).

S27. Han, S.H. & Lee, J.Y. Spatial separation of sensitizer and fluorescent emitter for high quantum efficiency in hyperfluorescent organic light-emitting diodes. *J. Mater. Chem. C* **6**, 1504–1508 (2018).

S28. Jeon, S.K., Park, H.-J. & Lee, J.Y. Highly efficient soluble blue delayed fluorescent and hyperfluorescent organic light-emitting diodes by host engineering. *ACS Appl. Mater. Interfaces* **10**, 5700–5705 (2018).